



Temperature-controlled synthesis and photocatalytic properties of ZnO–SnO₂ nanocomposites

Pongthep Jansanthea¹ · Jaratpong Kanthabangharn¹ · Weerasak Chomkitichai¹ · Jiraporn Ketwaraporn¹ · Chaluy Saovakon¹ · Chaowarit Wansao² · Aimon Wanaek² · Parinya Kraivuttinun³ · Pusit Pookmanee^{4,5} · Sukon Phanichphant⁶

Received: 21 July 2020 / Revised: 27 October 2020 / Accepted: 14 January 2021 / Published online: 19 January 2021

© Australian Ceramic Society 2021

Abstract

The objective of this work was the synthesis of a zinc oxide-tin oxide (ZnO–SnO₂; ZT) nanocomposite while controlling the growth structure with the calcination temperature and the photocatalytic degradation of a rhodamine B (RhB) dye solution. Zinc acetate, tin chloride, and sodium hydroxide were used as the precursor. In the study of the effect of the reaction temperature on the synthesis, the synthesis of the ZT nanocomposite had a temperature change in the range of 300–800 °C when the mole ratio of the precursors and other factors were held constant. The effect of the synthesis reaction temperature on the photocatalytic activity was examined. The synthesized samples were characterized by X-ray diffraction (XRD), scanning electron microscopy (SEM), energy-dispersive spectroscopy (EDS), Fourier transform infrared spectroscopy (FTIR), UV–vis diffuse reflectance spectroscopy (UV–DRS), and photoluminescence (PL) spectroscopy. Results showed that the synthesized ZT nanocomposites consisted of hexagonal ZnO and tetragonal SnO₂. The content of SnO₂ in the sample increased evidently with increasing reaction temperature. The experimental findings showed that increasing the reaction temperature resulted in favorable chemical and physical properties for the ZT nanocomposite photocatalytic reactions, such as high-purity phases, high crystallinity, and lower rates of electron–hole pair recombination. RhB was used as the representative pollutant for evaluating the photocatalytic activity under UV illumination. The ZT nanocomposite synthesized at 800 °C showed the highest photodegradation efficiency of 79.53% and a first-order kinetic rate constant of 0.0139 min^{−1} in 120 min. The most influential factors affecting the photocatalytic activity were the phase proportions and the phase purity of the ZT nanocomposite, which were controlled via the calcination temperature.

Keywords ZnO–SnO₂ · Temperature control · Photocatalytic · Rhodamine B

✉ Pongthep Jansanthea
pongthep.jan@uru.ac.th

¹ Program in Chemistry, Faculty of Science and Technology, Uttaradit Rajabhat University, Uttaradit 53000, Thailand

² Program in Physics, Faculty of Science and Technology, Uttaradit Rajabhat University, Uttaradit 53000, Thailand

³ Program in Environmental Science, Faculty of Science and Technology, Uttaradit Rajabhat University, Uttaradit 53000, Thailand

⁴ Program in Applied Chemistry, Faculty of Science, Maejo University, Chiang Mai 50290, Thailand

⁵ Nanoscience and Nanotechnology Research Laboratory (NNRL), Faculty of Science, Maejo University, Chiang Mai 50290, Thailand

⁶ Materials Science Research Center, Faculty of Science, Chiang Mai University, Chiang Mai 50200, Thailand

Introduction

In the past several decades, many semiconductor metal oxides have attracted increasing attention in the wide variety of applications, such as environmental monitoring, air quality control, gas sensors, and photocatalysis in air and water purification treatments [1, 2]. Zinc oxide (ZnO) and tin oxide (SnO₂) are *n*-type wide band gap semiconductors ($E_g = 3.37$ and 3.6 eV, respectively), making them interesting candidates for the development of future materials due to their wide range of applications [3, 4]. Among the nanomaterials used for photocatalysis, those materials synthesized of ZnO and SnO₂ are important semiconductor materials with large direct band gaps and high exciton binding energies. They also have good stability and are low cost and non-toxic [5, 6]. However, the disadvantage of a pure semiconductor photocatalyst is that the rapid recombination of photo-produced electrons and holes in

the semiconductors significantly reduces the efficiency of photocatalytic reaction, resulting in the decreased efficiency of the photocatalytic reactions. A solution to this problem is the coupling of two semiconductors, which results in good chemical and physical properties [7].

In the last decades, some complex oxides, including ZnO-SnO₂, have attracted wide interest with due to the possibility of optimizing the physical and chemical properties of the photocatalyst. A ZnO-SnO₂ nanocomposite exhibits a higher photo response than pure ZnO or SnO₂ [8]. Accordingly, the addition of ZnO to SnO₂ will generate useful composite nanostructures [9]. In the case of coupled semiconductors, the photocatalytic efficiency depends largely upon the location of the valence band (VB) and conduction band (CB) edges. The CB edge of ZnO is more negative than that of SnO₂, which makes SnO₂ the better candidate for accepting electrons from the CB of ZnO, whereas the VB edge of ZnO is less positive than that of SnO₂, which favors the transfer of holes from the VB of SnO₂ to the VB of ZnO. This whatever is most suitable as a descriptor result in better charge separation, which leads to an increase in photocatalytic efficiency [10]. The ratio between ZnO and SnO₂ is also important to the photocatalytic reaction efficiency. Most researches were conducted by setting the concentrations of precursors in different proportions [3, 11].

In the present study, we report on a ZT nanocomposite synthesized via chemical precipitation and control the proportion of ZnO:SnO₂ by using calcination processes at different temperatures. The synthesized samples will be investigated in terms of their chemical, physical, and optical properties. The photocatalytic degradation of RhB dye solution over the ZT nanocomposite is investigated to demonstrate potential applications. In addition, a possible growth mechanism for the ZT nanocomposite is proposed. Finally, the photodegradation mechanism of the ZT nanocomposite is discussed.

Materials and methods

Materials

All chemicals were analytical reagent grade and used without any further purification. The deionized (DI) water was used for solution preparation. The reagents consisted of zinc acetate dihydrate (99.5%, LOBA Chemie, India), tin(II) chloride (98.0%, Kemaus, Australia), sodium hydroxide (98.0%, LOBA Chemie, India), hydrochloric acid (35.4%, LOBA Chemie, India), and rhodamine B (99.5%, LOBA Chemie, India).

Synthesis and characterization

Nanocrystalline stoichiometric ZT samples were synthesized from 0.05 M aqueous solution of zinc acetate dihydrate (Zn(CH₃COO)₂·2H₂O) and tin(II) chloride dihydrate

(SnCl₂·2H₂O). Zn(CH₃COO)₂·2H₂O was dissolved in 100 mL of DI water, while SnCl₂·2H₂O was dissolved in 20 mL of conc. HCl and diluted to 100 mL with DI water. Next, these two mixtures were mixed together using a 1:1 mol ratio and stirred for about 30 min. Afterwards, 0.1 M NaOH solution was slowly added dropwise to the homogeneous mixture with constant stirring to complete precipitation. The precipitate was obtained, filtered, and then dried at 80 °C for 24 h. Finally, the powder was calcined at 300, 600, and 800 °C for 12 h. The synthesized samples were labeled according to their calcination temperatures as ZT-300, ZT-600, and ZT-800, respectively. For pure ZnO and SnO₂, separate precipitates were obtained via the same process and finally calcined at 600 °C for 12 h.

The phase transitions of the final samples were studied via X-ray diffractometer (JEOL, JDX-3530, Japan). The morphologies and chemical compositions of the synthesized samples were investigated by scanning electron microscope (JEOL, JSM 5410LV, Japan) and energy-dispersive spectrometer (Oxford, Inca 6647, England). The functional groups of sample powder were identified via a Fourier transform infrared spectrometer (Perkin Elmer, Spectrum RX I, England). The band gap energy was recorded using a UV–vis diffuse reflectance spectrophotometer (Shimadzu, UV-3101PC, Japan). The electronic structures of the samples were investigated via photoluminescence spectrometer (AVANTES, AvaSpec-2048TECH, Netherlands).

Photocatalytic studies

The photocatalytic activities of the final samples were studied under UV irradiation. Rhodamine B (RhB) was chosen as the representative dye pollutant with which to evaluate the photocatalytic activity of the synthesized sample. The evolution of the initial concentration of 2×10^{-6} M RhB was followed through the evolution of the characteristic wavelength at 554 nm. The photocatalytic experiments were carried out in 100-mL glass reactors containing 50 mL of RhB solution and 0.050 g of ZT photocatalyst. The reactor was covered by a black wall box to prevent external radiation. Similar UV irradiation was provided by two 6-W UV tube lamps with short waves of 254 nm UV-C (Sylvania, G6W, Japan) from vertical positions on both sides of the reactor. The schematic diagram of the photocatalytic set-up is shown in Fig. 1. In each test, the reaction had to reach chemical adsorption–desorption equilibrium via continuous stirring for 60 min in the black wall box without external illumination. Afterwards, each solution was irradiated under UV light with continuous magnetic stirring. A fixed quantity of the solution (3 mL) was removed at preset time intervals of about 0, 15, 30, 45, 60, 90, and 120 min. Then, the sample was filtered through a 0.22- μ m syringe filter (MS® MCE Syringe filter, Membrane Solution, USA). The concentration of RhB solution was determined by UV–vis spectrophotometer (T90+, PG Instruments, UK).

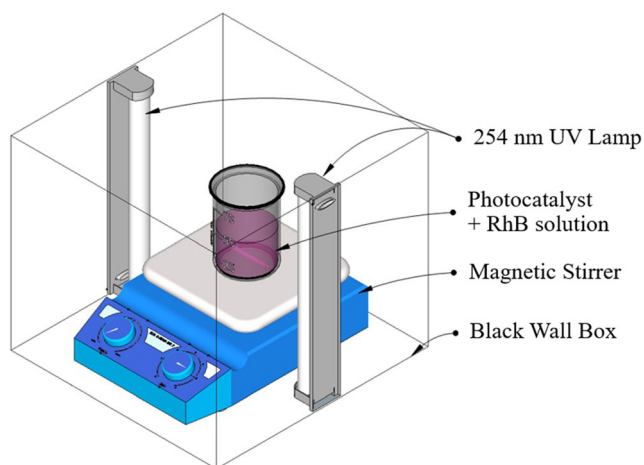


Fig. 1 Schematic diagram of the photocatalytic set-up

Results and discussion

Characterizations of the ZT nanocomposites

XRD analysis

The X-ray diffraction patterns of the ZT nanocomposite samples are shown in Fig. 2. As can be seen, all reflections correspond to crystalline ZnO and SnO₂, in accordance with the Joint Committee on Powder Diffraction Standards (JCPDS) file no. 01-079-0205 and file no. 00-002-1337, respectively. The main characteristic peaks at 2θ values of 31.98°, 34.66°, 36.48°, 47.75°, and 56.81° correspond to the (100), (002), (101), (102), and (110) diffraction planes of hexagonal ZnO, respectively. The diffraction peaks at 26.92°, 34.11°, 38.17°, 52.11°, 54.94°, and 58.21° belong to the (110), (101), (200), (211), (220), and (002) diffraction planes of tetragonal SnO₂,

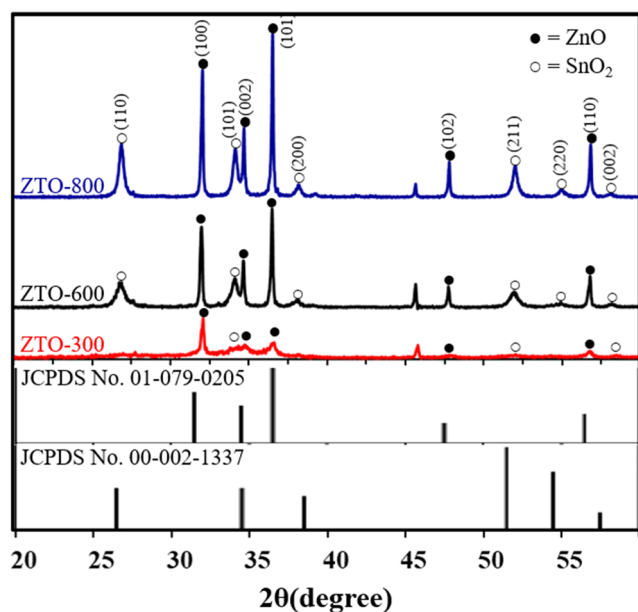


Fig. 2 XRD patterns for the ZT nanocomposite

respectively. No peaks corresponding to other phases, such as SnO, Sn(OH)₂, or ZnSn(OH)₆, were found. Additional peaks at 46.13° could not be identified as the phases of any possible compounds, consistent with previous reports [12]. For ZT-300, the intensities of the diffraction peaks assigned to tetragonal SnO₂ were very small. As the temperature increased to 600 °C, the characteristic peaks of the SnO₂ phase became more evident and had greater intensity. Peak intensities corresponding to the ZnO and SnO₂ phases also increased with increases in the calcination temperature. The approximate trend ratio can be obtained from the relative intensity ratio method [13]. The percentage of the SnO₂ phase was calculated based on the normalized ratio of the relative intensity for the (211) peak of SnO₂ to that for the (101) peak of ZnO. The calculated percentages for the SnO₂ phase were 6.55, 11.83, and 24.50% for ZT-300, ZT-600, and ZT-800, respectively. The average nano-crystallite sizes (*D*) were calculated using the Debye–Scherrer's equation [14]. The average crystallite sizes of the synthesized ZnO and SnO₂ were calculated using the most intense peak (101) and (110) planes of ZnO and SnO₂, respectively. The average crystallite sizes of ZnO were found to be 13.18, 79.47, and 94.07 nm for ZT-300, ZT-600, and ZT-800, respectively. The average crystallite sizes of SnO₂ were found to be 18.44 and 33.58 nm for ZT-600 and ZT-800, respectively. It was not possible to calculate the crystallite sizes of SnO₂ for the ZT-300 sample due to a very low signal. These results indicate that an increase in the calcination temperature increases the average crystalline sizes and crystallinities of the ZnO and SnO₂ phases.

SEM and EDS analyses

The SEM micrographs of the ZT nanocomposite samples are shown in Fig. 3. In terms of morphology, ZT-300 consists of spherical-like, needle-like, and agglomerate particles. In the case of ZT-600, the particles are granular, uniform, and better distributed than those of ZT-300. Furthermore, the ZT-800 particles are irregular in shape and have a high degree of agglomeration. The EDS spectra and elemental contents of the ZT nanocomposites are shown in Fig. 4. They confirm the presence of Zn, Sn, and O on the ZT nanocomposite samples. From the table in Fig. 4, it was found that the weight percentage of Sn increases with increasing calcination temperature. This result was consistent in an increase in SnO₂ phase from the XRD results, and similar to the synthesis results obtained by preparing with a higher Sn ratio [15].

FTIR analysis

The functional groups of the synthesized ZT nanocomposites were examined using FTIR spectroscopy in the range of 400–4000 cm⁻¹ at room temperature, and the results are presented in Fig. 5. The observed FTIR spectrums exhibit various well-

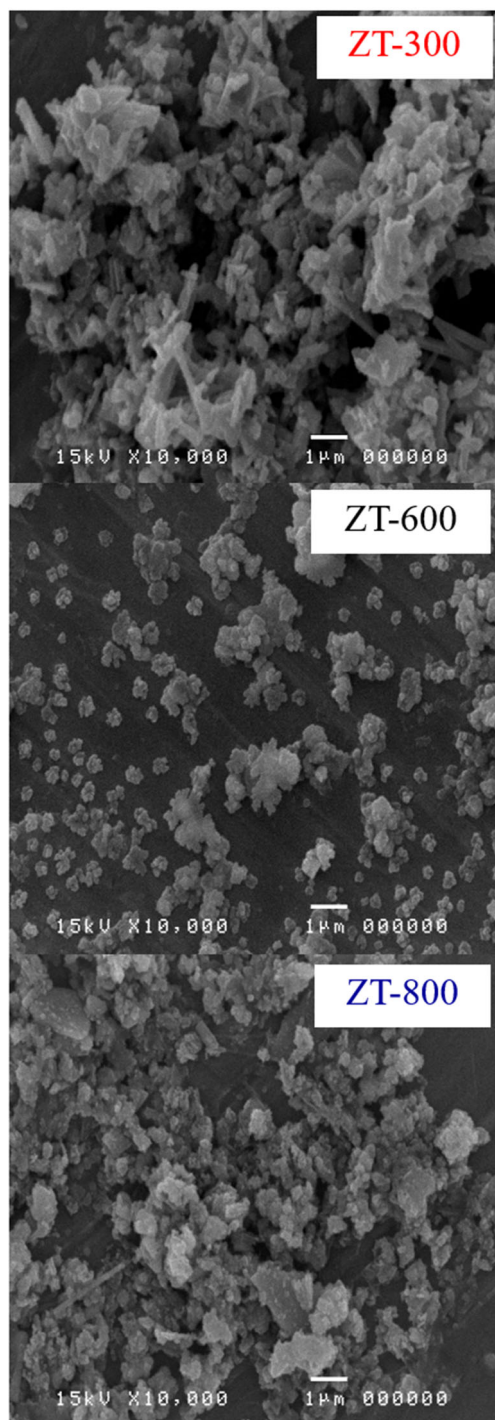


Fig. 3 SEM images of the ZT nanocomposites

defined absorption bands at 490, 670, 912, 1044, 3452, and 3494 cm^{-1} . As can be seen, the appearance of a peak at 490 cm^{-1} clearly indicates the formation of ZnO nanoparticles, which is corroborated by Nagaraju [16]. Absorbance bands around 620–670 cm^{-1} could be attributed to the framework vibrations of tin oxide [17]. It is clear that absorbance bands at 490 and 670 cm^{-1} that contribute to Zn–O and O–Sn–O appear in the IR spectrum of synthesized ZT samples,

confirming the presence of the ZnO and SnO₂ nanocomposites. The observed broad peaks at 530 cm^{-1} are due to possible vibrations of Sn–O modes [18]. The bonds in the wavelength ranging from 912 to 1044 cm^{-1} are ascribed to the bending of the Sn–OH bonds, and the peaks at 3452–3494 cm^{-1} come from the stretching mode vibrations of OH [11, 19]. Thus, the FTIR spectra confirmed that the Sn–O bonds and OH groups resulting from the phase transformation of Sn(OH)₂ to SnO₂ are not yet completely present in all cases [20, 21]. No significant peak corresponding to the Sn–OH bonds is observed in the ZT nanocomposite calcined at 800 °C. The ZT-800 sample showed that higher purity ZnO–SnO₂ phases are possible when the ZT nanocomposite is calcined at higher temperatures.

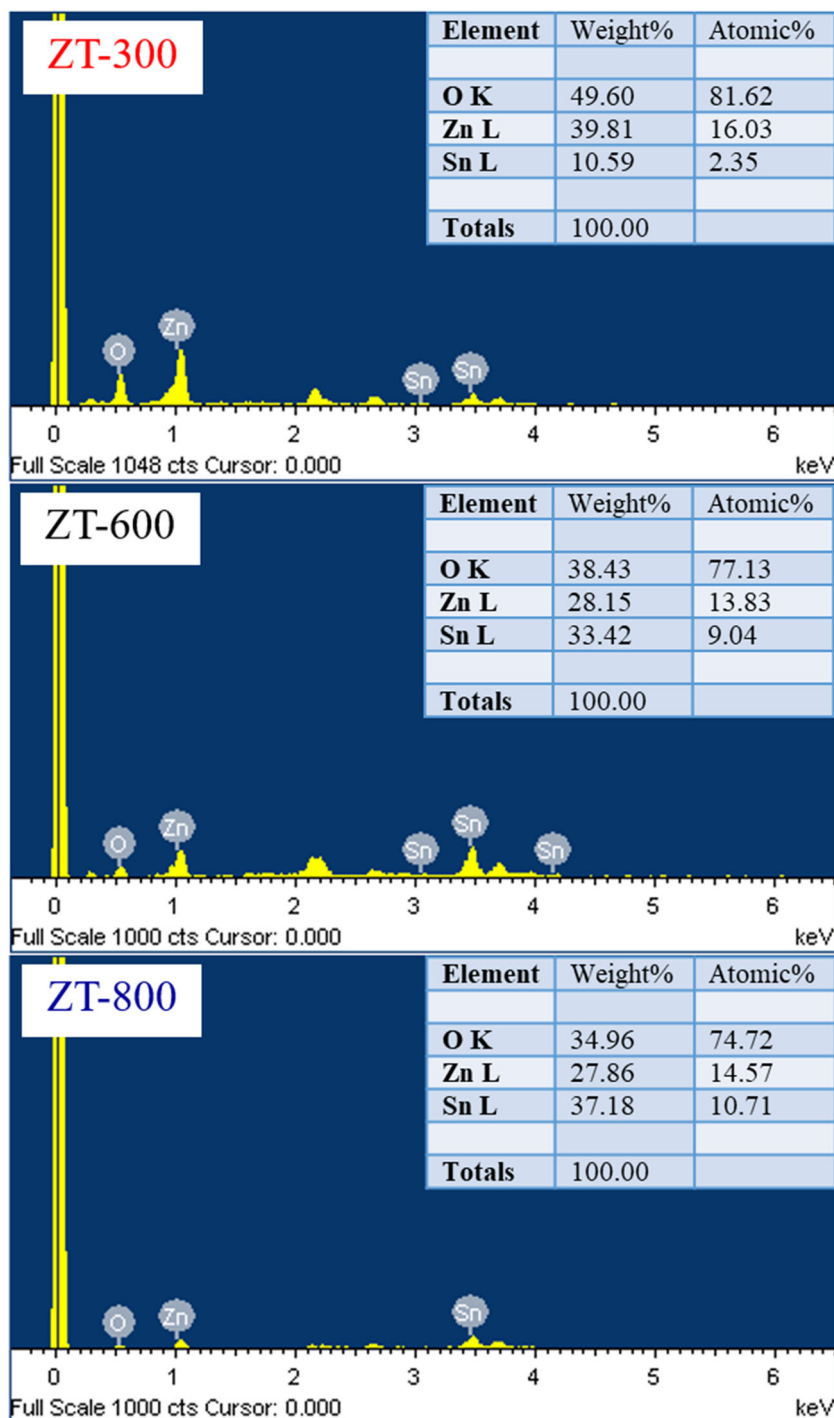
Optical analyses

The optical absorption properties of the synthesized ZT nanocomposites were studied by employing UV–vis diffusion reflectance analysis, as shown in Fig. 6. Figure 6 shows the broad absorption spectra of the ZT nanocomposite samples synthesized at different calcination temperatures. The characteristic peak of pure ZnO at 375 nm is where a sharp decrease in absorption, i.e., the absorption band edge, appears [22, 23]. This peak reveals the formation of ZnO and can be explained by the transition of electrons from the VB to the CB, thus leading to the intrinsic band gap absorption of ZnO [24]. The UV–vis absorption spectrum of pure SnO₂ showed a peak at around 270 nm. All the ZT nanocomposite samples showed strong adsorptions in the UV region around 270 and 375 nm. An exciton absorption at 375 nm was observed in the absorption spectrum for ZnO. In a direct band gap semiconductor where the wave vector is conserved, there is a relationship between the adsorption coefficient (α) near the absorption edge and the optical band gap (E_g). When the two oxides, for example, ZnO and SnO₂, are direct band gap semiconductors, the energy band gap of, for example, ZnO–SnO₂, can be determined. As such, the optical band gaps of the ZT nanocomposites were calculated using the following relation [25, 26]:

$$(\alpha h\nu)^2 = A(h\nu - E_g) \quad (1)$$

where A relates to the effective masses associated with the valence and conduction bands, α is the optical absorption coefficient, h is the Planck's constant, ν is the frequency of the photons, and E_g is the band gap energy. The optical band gap for the absorption edge can, therefore, be obtained by extrapolating the linear portion of $(\alpha h\nu)^2 - h\nu$ to $\alpha = 0$, as shown in Fig. 7. The energy band gaps of ZT-300, ZT-600, and ZT-800 are 3.30, 3.48, and 3.41 eV, respectively. The energy band gaps of the ZT nanocomposites were lower than those for pure ZnO and pure SnO₂. For the case of the ZT-300, it has the lowest band gap which does not follow the trend due to the presence of SnO phase in the composite materials. The presence of the SnO phase in the composite materials results

Fig. 4 EDS spectra of the ZT nanocomposites



in good optical properties because the SnO phase exhibits *p*-type conductivity, an indirect band gap of approximately 0.7 eV and a direct band gap of 2.7 eV [27].

Figure 8 shows the PL spectra of ZnO, SnO₂, and the ZT nanocomposites synthesized at different calcination temperatures. The PL spectra with excitations at 325 nm were analyzed to confirm the optical properties of the samples. The PL spectrum of pure ZnO shows UV emissions located at 386, 485, and 530 nm. A strong emission peak at 386 nm

corresponds to the near band-edge emission [28–30]. The emission peaks at 485 and 530 nm are attributed to the recombinations of holes in the valence band with electrons [22]. The pure SnO₂ sample also exhibited emissions at 485 and 530 nm, but the intensities are lower than those for pure ZnO. All the ZT nanocomposite samples exhibited sharp emission peaks around 386, 485, and 530 nm. The UV emission peaks at 386 nm correspond to the NBE emissions caused by electron transitions from the CB to the VB or exciton

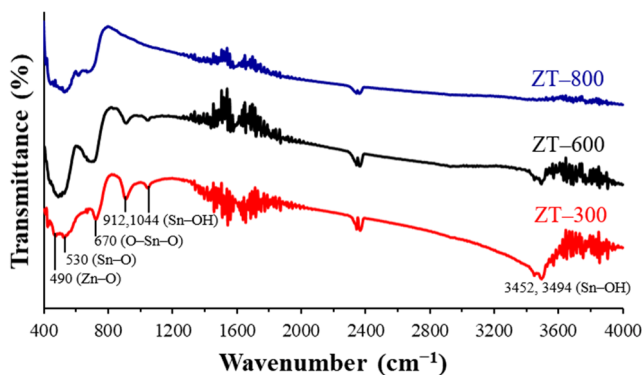


Fig. 5 FTIR spectra of the ZT nanocomposites

recombinations. The visible emission peaks at 485 and 530 nm are mainly related to intrinsic defects or impurities in the ZnO–SnO₂ [2, 25, 31, 32]. Defects in semiconductor nanocrystals have a strong influence on the electrical properties and photocatalytic activity of the material [33]. Photoluminescence in semiconductor materials arises from the energy emitted during the electron–hole recombination process. Consequently, a decrease in photoluminescence intensity is an indicator of an inhibited electron–hole recombination process [34].

Photocatalytic activities of the ZT nanocomposites

The evaluation of the photocatalytic behavior of the ZT nanocomposites under UV irradiation was carried out through the degradation of the RhB solution. The results are shown in Fig. 9. Figure 9a shows the measured RhB degradation efficiency as a function of reaction time for the experiments performed in the absence (photolysis) and presence of the ZT nanocomposites (photocatalysis). The equation used to calculate the degradation efficiencies for the treatment experiments was [35]

$$\text{Degradation (\%)} = [(C_0 - C_t) / C_0] * 100 \quad (2)$$

where C_0 and C_t are the initial and final concentrations of the RhB dye (M) in solution, respectively. Final RhB degradation values of 20.00, 65.45, 64.00, 62.88, 73.44, and 79.53% were observed for photolysis, ZnO, SnO₂, ZT-300, ZT-600, and ZT-800, respectively (Fig. 9a). The photocatalytic activity of ZT-800 was the highest after illumination for 120 min at 79.53%. A comparison of the kinetics of the ZT nanocomposites obtained at different calcination temperatures showed that the calcination temperature has an influence on the kinetics of these nanocomposites. The kinetic parameters of the RhB degradation follow the pseudo-first-order kinetic law [15]:

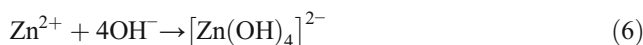
$$\ln(C_0/C_t) = kt \quad (3)$$

where k and t are the rate constant (min^{-1}) and reaction time (min), respectively. The kinetic curves and relative rate constant values are displayed in Fig. 9b. The kinetic rate constant values for photolysis, ZnO, SnO₂, and the ZT-300, ZT-600, and ZT-800 photocatalysts are 0.002, 0.0085, 0.0081, 0.0075, 0.0112, and 0.0139 min^{-1} , respectively. The highest kinetic rate constant is obtained by the ZT-800 photocatalyst. It can be seen that the photocatalytic abilities of the samples have the following order: ZT-800 > ZT-600 > ZnO > SnO₂ > ZT-300 > photolysis.

In this experiment, we controlled the synthesis of the ZnO/SnO₂ phases in the ZT nanocomposites by controlling the calcination temperature. The formation of the ZnO–SnO₂ structure in an alkaline solution is generally accepted to proceed according to the following chemical processes, where Zn²⁺ and Sn²⁺ ions are formed separately through the dissolution of Zn(CH₃COO)₂ and SnCl₂ in DI water:



In the initial stage of the precipitation, Zn²⁺ and Sn²⁺ react with OH[−] and produce the Zn(OH)₄^{2−} (Eq. 6) and Sn(OH)₂ (Eq. 7) complexes, respectively [12, 36]:



With calcination at 300 °C, the Zn(OH)₄^{2−} and Sn(OH)₂ complexes transform to the brownish powders of the ZnO and SnO phases, respectively (Eqs. 8–9). Generally, SnO is a black powder [37] that turns the sample powder darker when combined with the white ZnO powder. At this stage, a small amount of SnO₂ can occur, as in Eq. 10 [12].

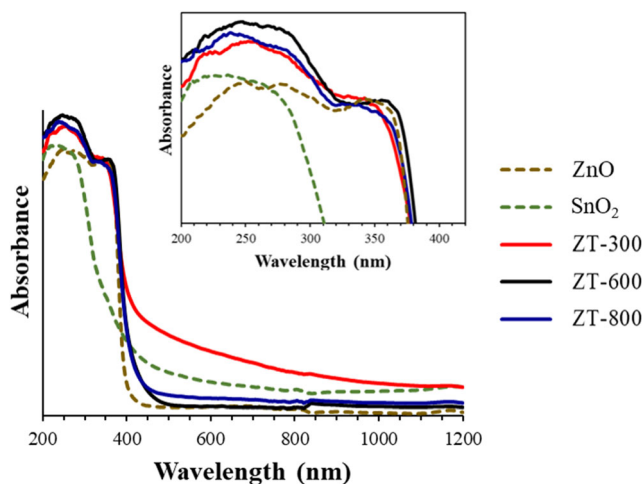


Fig. 6 Absorbance spectra of the ZT nanocomposites and their magnified 200–400 nm emission ranges

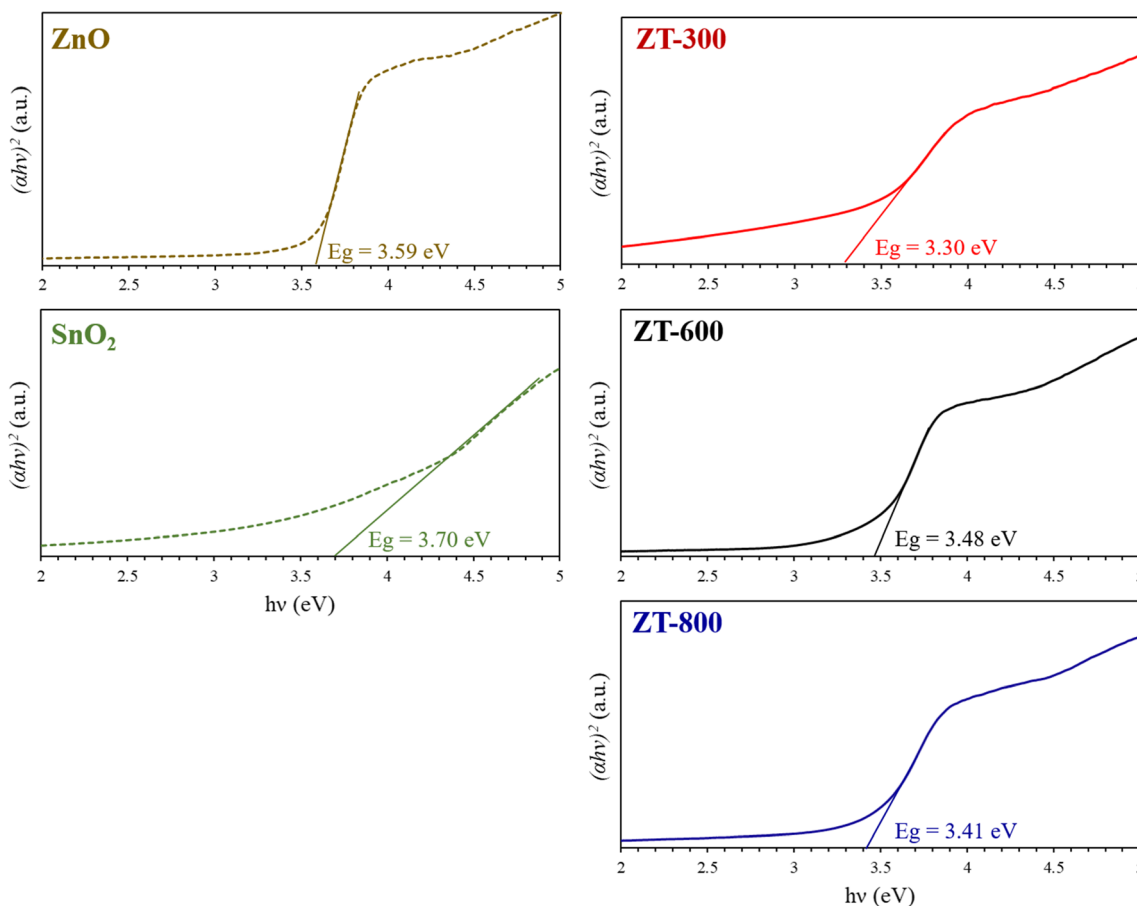
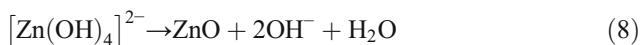


Fig. 7 Band gap energies of the ZT nanocomposites estimated via the plots of $(Ah\nu)^2$ vs. photon energy ($h\nu$)



When the temperature rises to 600 °C, the color of the sample changes from brown to light yellow, which indicates the change from SnO to SnO₂. In the FTIR results for 600 °C, Sn-OH bonds are still evident, indicating that the phase transition

from the Sn²⁺ precursor to the final SnO₂ is not complete. In the case of calcination at 800 °C, the pure white ZnO–SnO₂ structure is formed according to Eqs. 11–12 below [12, 38]. The possible formation processes for the samples synthesized at different calcination temperatures are shown in Fig. 10.

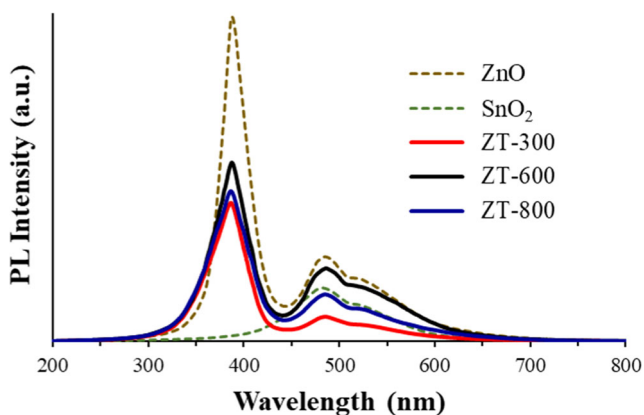
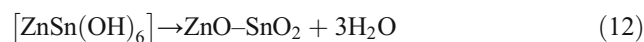
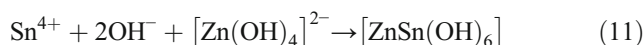


Fig. 8 Photoluminescence spectra of the ZT nanocomposites

When a ZT nanocomposite is activated using UV light, the photogenerated electrons transfer from the VB to the CB, whereas the positive holes move in the opposite direction (Eq. 13). In other words, electrons move from the CB of ZnO to the CB of SnO₂, whereas the holes move from the VB of SnO₂ to the VB of ZnO. As a result, almost all the photogenerated electrons and holes gather in the CB of SnO₂ and the VB of ZnO, respectively. Electrons and holes that migrate to the surfaces of the ZT nanocomposites will react with oxygen (O₂) and hydroxides/water (OH/H₂O) to form superoxide anion radicals ($\bullet\text{O}_2^-$) (Eq. 14) and hydroxyl radicals ($\bullet\text{OH}$), as shown in Eq. 14 and Eq. 15, respectively. Furthermore, $\bullet\text{O}_2^-$ can react with H₂O to create $\bullet\text{OH}$; see Eqs. 16–18. Both active $\bullet\text{O}_2^-$ and $\bullet\text{OH}$ species can degrade RhB

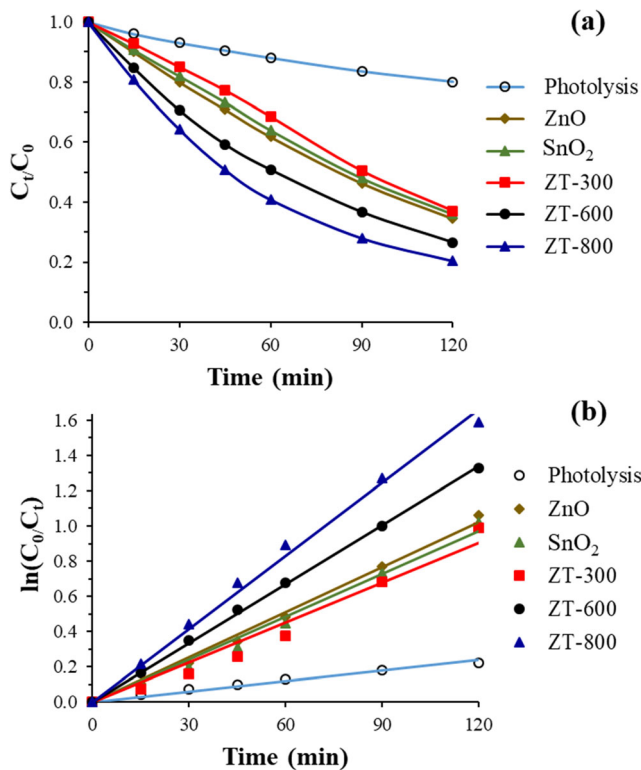
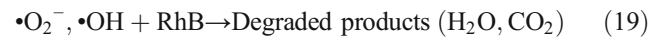
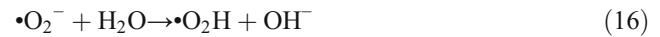
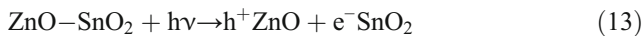


Fig. 9 Photocatalytic efficiencies (a) and first-order plots (b) for the degradation of the RhB solution by ZT nanocomposites under UV irradiation

into the final products H_2O and CO_2 (Eq.19) [10, 15, 32]. A schematic illustration of the photocatalytic activity over ZT nanocomposites under UV irradiation is shown in Fig. 11.



For Fig. 11, the VB and CB edges of ZnO and SnO₂ were calculated via the following equations [10, 39]:

$$E_{CB} = \chi - E_e - 0.5E_g \quad (20)$$

$$E_{VB} = \chi - E_e + 0.5E_g \quad (21)$$

where χ is the electronegativity (5.79 eV and 6.25 eV for ZnO and SnO₂, respectively), and E_e is the energy of free electrons on the hydrogen scale (~ 4.5 eV). The E_g of ZnO is 3.59 eV, and that for SnO₂ is 3.70 eV. The CB potentials of ZnO ($E_{CB(ZnO)}$) and SnO₂ ($E_{CB(SnO_2)}$) are calculated to be -0.505 and -0.100 eV vs. NHE, respectively. The related E_{VB} values of ZnO ($E_{VB(ZnO)}$) and SnO₂ ($E_{VB(SnO_2)}$) are calculated to be $+3.085$ and $+3.600$ eV vs. NHE, respectively. The ZnO-SnO₂ composites exhibit higher photocatalytic activity than pure SnO₂ and pure ZnO. According to the potential energy differences between ZnO and SnO₂, $E_{CB(ZnO)}$ is more negative than $E_{CB(SnO_2)}$, which makes SnO₂ a better candidate for accepting electrons from the $E_{CB(ZnO)}$, whereas $E_{VB(SnO_2)}$ is more positive than $E_{VB(ZnO)}$, which favors the transfer of holes from the VB of SnO₂ to the $E_{VB(ZnO)}$ [15]. With this mechanism, the composite ZnO-SnO₂ nanomaterial is very useful in separating electrons and holes, thus increasing carrier lifetimes and preventing recombinations [32]. For this reason, composite materials have an advantage over pure

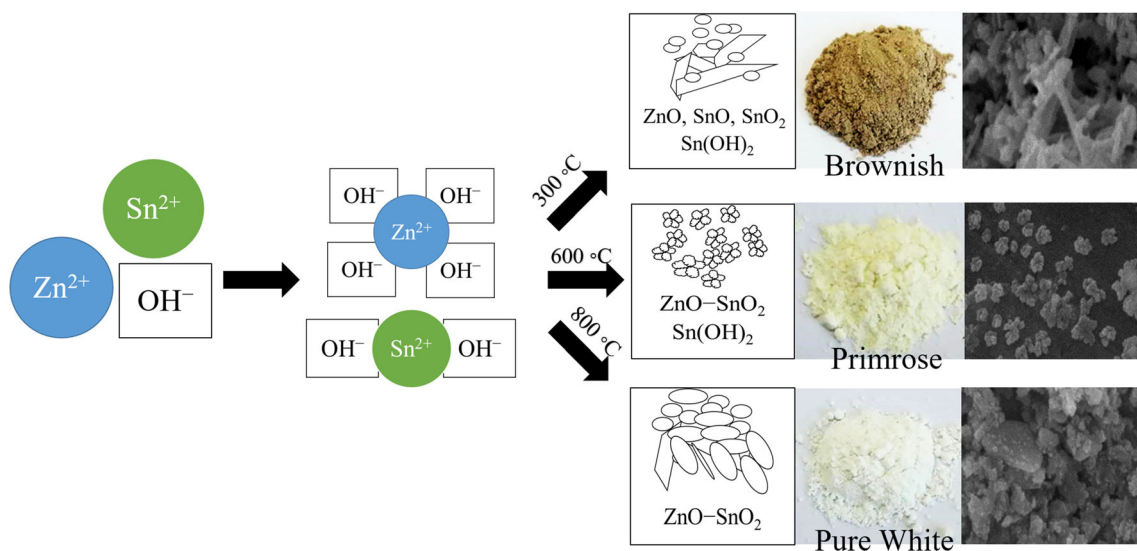
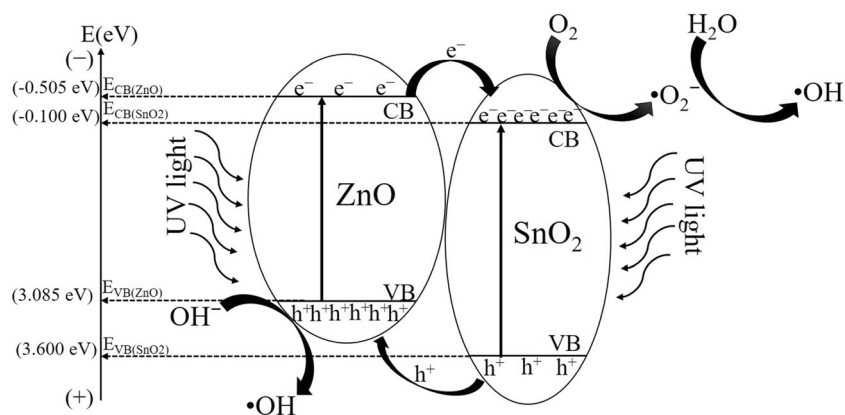


Fig. 10 Schematic diagram of the possible formation processes for the samples synthesized at different calcination temperatures

Fig. 11 A schematic diagram of the photodegradation of ZT nanocomposites under UV irradiation



materials in terms of photocatalytic reactions [11]. Many previous reports have shown that the photocatalytic activities of composites are much higher than those of pure semiconductor photocatalysts [7, 15].

When comparing the effect of synthesis temperature on the photocatalytic efficiency of ZT nanocomposite, the results indicate that the efficiency increases when the calcining temperature increases, which is consistent with a previous report [11]. This relationship may be due to the lower band gap energies, higher crystallinities, and phase purities of the samples. The enhanced photocatalytic efficiency of the ZT-800 sample calcined at higher temperatures is due to better crystallinity and the formation of a pure composite phase that inhibits the recombination of electron–hole pairs [10]. In contrast, ZT-300 had a lower photocatalytic efficiency than pure ZnO or pure SnO₂. The powder obtained through calcination at 300 °C showed possible phases of ZnO, SnO, SnO₂, and Sn(OH)₂ with very low crystallinities. Evidence that the SnO phase occurs in the ZT-300 sample can be found in the resulting brownish powder and the lower band gap energy when compared with other samples, corresponding to results reported by Salah [40]. The ZT-300 sample had the lowest photocatalytic efficiency despite its good optical properties, which may have been due to its lower crystallinity and many impurity phases.

Conclusions

In this work, ZT nanocomposites were obtained via the chemical precipitation subsequent by calcination process, and tested as a photocatalyst for degradation of RhB under UV light irradiation. The different calcination temperatures were used to synthesize ZT nanocomposites under a constant molar ratio of precursors. The synthesis conditions of this method can be produced from the optimum phase proportion and high-purity phases of ZT nanocomposites. For environmental applications, the degradation of the cationic dye RhB is possible in the presence of a ZT nanocomposite acting as a photocatalyst under UV irradiation. The results indicated that the photocatalysis process in the presence of a ZT nanocomposite synthesized at 800 °C for 12 h

offered the highest rate constant. On the basis of the results presented, the higher calcination temperature had potential effects on the photocatalytic properties of the samples such as high-purity phases, high crystallinity, and lower rates of electron–hole pair recombination. The composite material in this work demonstrated its potential for practical use. The work has also provided new guidelines for future improvements in, and development of, semiconductor materials for photocatalytic activities.

Acknowledgements The authors acknowledge the Program in Chemistry, Faculty of Science and Technology, Uttaradit Rajabhat University, Uttaradit, Thailand, for their research equipment.

Funding The authors received financial supports from the National Research Council of Thailand (NRCT).

References

1. Yang, X., Zhang, S., Yu, Q., Zhao, L., Sun, P., Wang, T., Liu, F., Yan, X., Gao, Y., Liang, X., Zhang, S., Lu, G.: One step synthesis of branched SnO₂/ZnO heterostructures and their enhanced gas-sensing properties. *Sens Actuator B Chem.* **281**, 415–423 (2019)
2. Khoang, N.D., Trung, D.D., Duy, N.V., Hoa, N.D., Hieu, N.V.: Design of SnO₂/ZnO hierarchical nanostructures for enhanced ethanol gas-sensing performance. *Sens Actuator B Chem.* **174**, 594–601 (2012)
3. da Silva, L.F., M'Peko, J.-C., Catto, A.C., Bernardini, S., Mastelaro, V.R., Aguir, K., Ribeiro, C., Longo, E.: UV-enhanced ozone gas sensing response of ZnO–SnO₂ heterojunctions at room temperature. *Sens Actuator B Chem.* **240**, 573–579 (2017)
4. Yu, L., Song, H., Tang, Y., Zhang, L., Lv, Y.: Controllable deposition of ZnO-doped SnO₂ nanowires on Au/graphene and their application in cataluminescence sensing for alcohols and ketones. *Sens Actuator B Chem.* **203**, 726–735 (2014)
5. Liang, Q., Qiao, F., Cui, X., Hou, X.: Controlling the morphology of ZnO structures via low temperature hydrothermal method and their optoelectronic application. *Mater Sci Semicon Proc.* **89**, 154–160 (2019)
6. Luque, P.A., Nava, O., Soto-Robles, C.A., Chinchillas-Chinchillas, M.J., Garrafa-Galvez, H.E., Baez-Lopez, Y.A., Valdez-Núñez, K.P., Vilchis-Nestor, A.R., Castro-Beltrán, A.: Improved photocatalytic efficiency of SnO₂ nanoparticles through green synthesis. *Optik* **206**, 164299 (2020)

7. Modirshahla, N., Hassani, A., Behnajady, M.A., Rahbarfam, R.: Effect of operational parameters on decolorization of acid yellow 23 from wastewater by UV irradiation using ZnO and ZnO/SnO₂ photocatalysts. *Desalination*. **271**, 187–192 (2011)
8. Yang, T., Gu, K., Zhu, M., Lu, Q., Zhai, C., Zhao, Q., Yang, X., Zhang, M.: ZnO–SnO₂ heterojunction nanobelts: synthesis and ultraviolet light irradiation to improve the triethylamine sensing properties. *Sens Actuator B Chem*. **279**, 410–417 (2019)
9. Kim, H.W., Na, H.G., Kwon, Y.J., Cho, H.Y., Lee, C.: Decoration of Co nanoparticles on ZnO–branched SnO₂ nanowires to enhance gas sensing. *Sens Actuator B Chem*. **219**, 22–29 (2015)
10. Upadhaya, D., Talinungsang, Kumar, P., Purkayastha, D.D.: Tuning the wettability and photocatalytic efficiency of heterostructure ZnO–SnO₂ composite films with annealing temperature. *Mater Sci Semicon Proc* **95**, 28–34 (2019)
11. Rashad, M.M., Ismail, A.A., Osama, I., Ibrahim, I.A., Kandil, A.–H.T.: Photocatalytic decomposition of dyes using ZnO doped SnO₂ nanoparticles prepared by solvothermal method. *Arab J Chem* **7**, 71–77 (2014)
12. Campo, C.M., Rodríguez, J.E., Ramírez, A.E.: Thermal behaviour of romarchite phase SnO in different atmospheres: a hypothesis about the phase transformation. *Heliyon*. **2**(5), e00112 (2016)
13. Bazant, P., Sedlacek, T., Kuritka, I., Podlipny, D., Holcapkova, P.: Synthesis and effect of hierarchically structured Ag–ZnO hybrid on the surface antibacterial activity of a propylene–based elastomer blends. *Materials*. **11**(3), 363 (2018)
14. Jiang, J., Shi, L., Xie, T., Wang, D., Lin, Y.: Study on the gas-sensitive properties for formaldehyde based on SnO₂–ZnO heterostructure in UV excitation. *Sens Actuator B Chem*. **254**, 863–871 (2018)
15. Lin, J., Luo, Z., Liu, J., Li, P.: Photocatalytic degradation of methylene blue in aqueous solution by using ZnO–SnO₂ nanocomposites. *Mat Sci Semicon Proc*. **87**, 24–31 (2018)
16. Nagaraju, G., Udayabhanu, Shivaraj, Prashanth, S.A., Shastri, M., Yathish, K.V., Anupama, C., Rangappa, D.: Electrochemical heavy metal detection, photocatalytic, photoluminescence, biodiesel production and antibacterial activities of Ag–ZnO nanomaterial. *Mater Res Bull* **94**, 54–63 (2017)
17. Zhan, S., Li, D., Liang, S., Chen, X., Li, X.: A novel flexible room temperature ethanol gas sensor based on SnO₂ doped polydiallyldimethylammonium chloride. *Sensors–BASEL*. **13**, 4378–4389 (2013)
18. Kaizra, S., Bellal, B., Louafi, Y., Trari, M.: Improved activity of SnO for the photocatalytic oxygen evolution. *J Saudi Chem Soc*. **22**, 76–83 (2018)
19. Wan, W., Li, Y., Ren, X., Zhao, Y., Gao, F., Zhao, H.: 2D SnO₂ nanosheets: synthesis, characterization, structures, and excellent sensing performance to ethylene glycol. *Nanomaterials–BASEL*. **8**, 112–131 (2018)
20. Malik, R., Tomer, V.K., Duhan, S., Nehra, S.P., Rana, P.S.: One-pot hydrothermal synthesis of porous SnO₂ nanostructures for photocatalytic degradation of organic pollutants. *Energy Environ Focus*. **4**, 340–345 (2015)
21. Selvi, N., Sankar, S., Dinakaran, K.: Interfacial effect on the structural and optical properties of pure SnO₂ and dual shells (ZnO;SiO₂) coated SnO₂ core–shell nanospheres for optoelectronic applications. *Superlattice Microst*. **76**, 277–287 (2014)
22. Wang, M., Luo, Q., Hussain, S., Liu, G., Qiao, G., Kim, E.J.: Sharply-precipitated spherical assembly of ZnO nanosheets for low temperature H₂S gas sensing performances. *Mat Sci Semicon Proc*. **100**, 283–289 (2019)
23. Regonia, P.R., Pelicano, C.M., Tani, R., Ishizumi, A., Yanagi, H., Ikeda, K.: Predicting the band gap of ZnO quantum dots via supervised machine learning models. *Optik*. **207**, 164469 (2020)
24. Radkar, R.N., Bhanvase, B.A., Barai, D.P., Sonawane, S.H.: Intensified convective heat transfer using ZnO nanofluids in heat exchanger with helical coiled geometry at constant wall temperature. *Materials Science for Energy Technologies*. **2**, 161–170 (2019)
25. Zargar, R.A., Bhat, M.A., Parrey, I.R., Arora, M., Kumar, J., Hafiz, A.K.: Optical properties of ZnO/SnO₂ composite coated film. *Optik*. **127**, 6997–7001 (2016)
26. Shi, J.–B., Wu, P.–F., Lin, H.–S., Lin, Y.–T., Lee, H.–W., Kao, C.–T., Liao, W.–H., Young, S.–L.: Synthesis and characterization of single-crystalline zinc tin oxide nanowires. *Nanoscale Res Lett* **9**, 210 (2014)
27. Suman, P.H., Felix, A.A., Tuller, H.L., Varela, J.A., Orlandi, M.O.: Comparative gas sensor response of SnO₂, SnO and Sn₃O₄ nanobelts to NO₂ and potential interferents. *Sens Actuator B Chem*. **208**, 122–127 (2015)
28. Li, Q., An, M., Li, D.: In situ growth of ZnO nanowire film on nanocrystalline zinc electrodeposit via a low-temperature hydrothermal reaction. *Results Phys*. **12**, 1446–1449 (2019)
29. Kortidis, I., Swart, H.C., Ray, S.S., Motaung, D.E.: Detailed understanding on the relation of various pH and synthesis reaction times towards a prominent low temperature H₂S gas sensor based on ZnO nanoplatelets. *Results Phys*. **12**, 2189–2201 (2019)
30. Wang, J., Shen, Y., Li, X., Xia, Y., Yang, C.: Synergistic effects of UV activation and surface oxygen vacancies on the room-temperature NO₂ gas sensing performance of ZnO nanowires. *Sens Actuator B Chem*. **298**, 126858 (2019)
31. Baitha, P.Kr., Manam, J.: Luminescence behavior of Eu³⁺ activated ZnO/SnO₂ nanocomposite phosphor. *Optik* **126**, 4916–4923 (2015)
32. Xu, L., Xian, F., Zhang, Y., Wang, W., Qiu, K., Xu, J.: Synthesis of ZnO–decorated SnO₂ nanopowder with enhanced photocatalytic performance. *Optik*. **194**, 162965 (2019)
33. Karunakaran, C., SakthiRaadha, S., Gomathisankar, P.: Photocatalytic and bactericidal activities of hydrothermally and sonochemically prepared Fe₂O₃–SnO₂ nanoparticles. *Mat Sci Semicon Proc*. **16**, 818–824 (2013)
34. Medhi, R., Li, C.–H., Lee, S.H., Marquez, M.D., Jacobson, A.J., Lee, T.–C., Lee, T.R.: Uniformly spherical and monodisperse antimony- and zinc-doped tin oxide nanoparticles for optical and electronic applications. *ACS Appl Nano Mater* **2**, 6554–6564 (2019)
35. Balakrishnan, G., Velavan, R., Batoo, K.M., Raslan, E.H.: Microstructure, optical and photocatalytic properties of MgO nanoparticles. *Results Phys*. **16**, 103013 (2020)
36. Hemmati, S., Firooz, A.A., Khodadadi, A.A., Mortazavi, Y.: Nanostructured SnO₂–ZnO sensors: highly sensitive and selective to ethanol. *Sens Actuator B Chem*. **160**, 1298–1303 (2011)
37. Wang, J., Li, H., Meng, S., Ye, X., Fu, X., Chen, S.: Controlled synthesis of Sn–based oxides via a hydrothermal method and their visible light photocatalytic performances. *RSC Adv*. **7**, 27024–27032 (2017)
38. Mondal, B., Basumatari, B., Das, J., Roychaudhury, C., Saha, H., Mukherjee, N.: ZnO–SnO₂ based composite type gas sensor for selective hydrogen sensing. *Sens Actuator B Chem*. **194**, 389–396 (2014)
39. Taufique, M.F.N., Haque, A., Karnati, P., Ghosh, K.: ZnO–CuO nanocomposites with improved photocatalytic activity for environmental and energy applications. *J Electron Mater*. **47**(11), 6731–6745 (2018)
40. Salah, N., AL–Shawafi, W.M., Habib, S.S., Azam, A., Alshahrie, A.: Growth-controlled from SnO₂ nanoparticles to SnO nanosheets with tunable properties. *Mater Des* **103**, 339–347 (2016)

Publisher's note Springer Nature remains neutral with regard to jurisdictional claims in published maps and institutional affiliations.